Broadband Fast-Wave Propagation in a Non-Foster Circuit Loaded Waveguide

Jiang Long, *Student Member, IEEE*, Minu M. Jacob, *Student Member, IEEE*, and Daniel F. Sievenpiper, *Fellow, IEEE*

***Abstract*—Frequency independent fast-wave (FW) propagation with phase velocity greater than the speed of light can be ideally realized in a dielectric medium whose relative permittivity is positive, but less than 1. Conventionally, FW propagation is implemented by non-TEM waveguides or antiresonance-based metamaterials, which suffers from the narrow bandwidth due to the dispersion. In contrast, non-Foster circuits provide a brand new method for reducing the dispersion so as to broaden the bandwidth. This paper demonstrates broadband FW propagation in a microstrip line that is periodically loaded with non-Foster circuits. Discrete transistor-based non-Foster circuits functioning as negative capacitors are successfully designed with the novel modified negative impedance converter circuits. A −10-pF negative capacitor over a bandwidth of 10–150 MHz has been implemented. The fabricated circuits have been integrated into a microstrip line to form a FW waveguide. The retrieved phase velocity of the effective medium from the measured S-parameters characterizes a stable and causal FW medium with constant phase velocity of $1.2c$ from 60 to 120 MHz, and this has been further verified by Kramers–Kronig relations and the near-field measurements along the waveguide. In conclusion, a stable, causal, and broadband FW waveguide has been achieved by means of transistor-based non-Foster circuits. The implemented broadband FW propagation can potentially be applied in broadband leaky-wave antennas and cloaking techniques.**

***Index Terms*—Fast-wave (FW), metamaterials, non-Foster circuits, periodically loaded transmission line.**

I. Introduction

THE applications relating to the manipulation of the electromagnetic (EM) wave propagation for antennas [1]–[5], cloaking devices [6], [7], and other microwave applications [8] need fast-wave (FW) propagation, where the phase velocity is faster than the speed of light in vacuum. As is well known, faster-than-light phase velocity can be easily realized by a non-TEM metallic waveguide and it has been applied to leaky-wave antennas [3], and super coupling and energy squeezing devices [8]. Also, metamaterials that support FW propagation, including composite right/left-hand (CRLH) structures [4], [5] and split-ring resonators (SRRs) [6], [7], have also been proposed. However, all these approaches for FW propagation are dispersive, which reduces the bandwidth of operation. Thus, it is desirable to find a method of implementing non-dispersive FW propagation such that the phase velocity can be faster than the speed of light and independent of frequency.

The dispersion in the conventional FW structures is attributed to the resonance. A non-TEM wave in a rectangular waveguide is dispersive due to its transverse resonance. All the other aforementioned realizations of the FW propagation [4]–[7] are also based on resonance. The reason why resonance is often used for faster-than-light phase velocity originates from the well-known equation

$$v_p = \frac{c}{\sqrt{\mu_r \times \epsilon_r}} \tag{1}$$

where c is the velocity of light in vacuum and ϵ_r and μ_r are the relative permittivity and permeability, respectively. The requirement of FW (i.e., $v_p > c$) dictates that at least one of ϵ_r and μ_r has to be less than 1. This property can be easily achieved with the negative slope of the reactance or susceptance in EM structures at their antiresonant frequencies. Nevertheless, the inverse relationship between the quality factor (Q) and the bandwidth of a resonance results in a tradeoff between the loss and the maximum achievable bandwidth.

Fortunately, resonance is not the only way to realize an ϵ_r or μ_r less than 1. A non-Foster circuit has an input impedance with a negative reactance/susceptance slope versus frequency, and consequently, it is able to compensate for the positive slope of a natural reactance/susceptance without utilizing any resonances. Thus, non-Foster circuits are good candidates to obtain broadband FW propagation.

In [9], Hrabar *et al.* designed a unit cell consisting of a negative capacitor attached to a short transmission line and simulated an EM cloak. In [10], we have shown the possibility of designing beam-squint-free leaky-wave antennas with non-Foster circuits. Both papers reported measurements on single unit cell and the multiple-unit-cell simulations for investigating the effects of the large-scale EM structures. The only available measurement of a multi-section FW structure was presented over the bandwidth of 2–40 MHz in [11] and [12], where the negative capacitors were realized with op-amp circuits. As is well known, an op-amp circuit is an integrated circuit (IC) whose available operating frequency is usually below 50 MHz owing to the fixed gain-bandwidth (GBW) product and its parasitics. In contrast, benefiting from the higher transition frequencies, transistor-based circuits can work at higher frequencies. Additionally, the transistor-based circuits are more desirable than op-amp circuits in integration, as the former possess less complexity and chip area-consumption. Therefore, transistor-based non-Foster

Manuscript received January 15, 2014; revised February 24, 2014; accepted February 25, 2014. Date of publication March 10, 2014; date of current version April 02, 2014.

The authors are with the Department of Electrical and Computer Engineering, University of California at San Diego (UCSD), La Jolla, CA 92093 USA (e-mail: jilong@ucsd.edu; mmjacob@ucsd.edu; dsievenpiper@eng.ucsd.edu).

Color versions of one or more of the figures in this paper are available online at http://ieeexplore.ieee.org.

Digital Object Identifier 10.1109/TMTT.2014.2309324

circuits earn more interests in realizing negative capacitors at higher frequencies, and thus the broadband FW applications.

In this paper, a discrete transistor-based negative capacitor circuit has been proposed and integrated into a microstrip line. A three-unit-cell loaded microstrip line has been successfully fabricated and tested. The retrieved effective material parameters from the measured S-parameters identify an effectively uniform medium with a constant (less than 10% variation) phase velocity of $1.2c$ over 60–120 MHz, or 2:1 bandwidth. Compared to [11] and [12], the central operating frequency has been increased from 20 to 90 MHz, and the bandwidth is still significantly more broadband than the conventional metallic waveguides. Furthermore, the measurement results have been verified by Kramers–Kronig relations and the measured near-field distribution along the microstrip line, which demonstrate that the accomplished waveguide can be regarded as a stable, causal, and homogeneous material rather than a lumped element. Thus, this paper shows the possibility of cascading multiple unit cells with transistor based non-Foster circuits to achieve an effectively homogeneous material that supports broadband FW propagation. The accomplished FW waveguide can potentially be applied in broadband beam-squint-free leaky-wave antennas and thin-film cloaking techniques [2].

This paper is organized as follows. Section I introduces the FW propagation and discusses the possibility of broadband FW propagation with non-Foster circuits. Section II presents the analytical calculation of the phase delay in a transmission line periodically loaded with negative capacitors. The design and measurement of the transistor-based negative capacitor circuit are detailed in Section III. The implementation and measurement of the integrated FW waveguide structure are shown in Section IV, including the fabrication, S-parameter measurement, the retrieved properties of the effective homogeneous material, the discussion on causality, and the near-field measurements. Section V draws a conclusion.

II. FW Propagation in a Periodically Loaded Transmission Line

FW propagation in a guided medium can be analyzed by using the basic transmission-line theory. The proposed FW waveguide consists of a microstrip line that is periodically loaded with negative capacitors, as illustrated in Fig. 1. The effective capacitance per unit length of an unloaded microstrip line can be easily derived from [13]. Provided that the negative capacitors have an absolute capacitance value that is smaller than the capacitance of the bare microstrip line, they reduce the net capacitance of the loaded microstrip line while keeping the total capacitance per unit length to be positive. Meanwhile, the inductance does not change. Consequently, the resultant phase velocity gets larger. Therefore, it is possible to have a faster-than-light phase velocity by properly choosing the negative capacitance.

To characterize the phase velocity accurately, the loaded microstrip line is modeled as general periodic structure with unit cells that are composed of a short transmission line and lumped capacitor. Therefore, it can be analytically studied based on the periodically loaded transmission-line theory, as detailed in [14] and [15]. The phase delay of one section of a loaded transmission line is obtained as

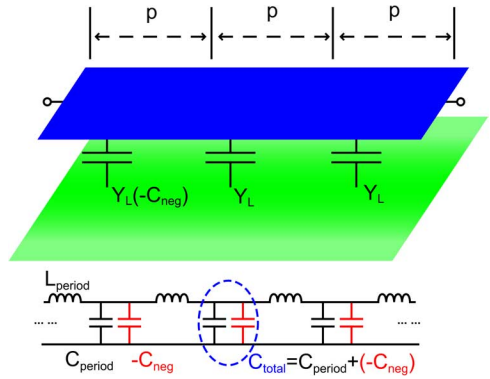

Fig. 1. Proposed FW propagation structure and its equivalent transmission-line model.

$$\theta = \arccos\left[\cos(kl) - \frac{Y_L}{2Y_0}\sin(kl)\right] \tag{2}$$

where k is the propagation constant of the unloaded microstrip line, l and Y_0 are the length of a section of the microstrip line (i.e., one unit cell) and its characteristic admittance, respectively, and Y_L is the admittance of the periodic load. According to Fig. 1, Y_L is a negative capacitor, and thus,

$$Y_L = -j\omega C_{\text{neg}}, (C_{\text{neg}} > 0). \tag{3}$$

The transmission line to be fabricated consists of a microstrip line that is 100-mm long (i.e., the length of three unit cells) and 10-mm wide on a 62-mil-thick FR-4 substrate ($\epsilon_r = 4.4$). The effective capacitance per unit cell, C_{period}, is calculated to be 10.0 pF, and the effective dielectric constant $\epsilon_{r,\text{eff}}$ is 3.7 [13]. Since C_{period} is proportional to $\epsilon_{r,\text{eff}}$, the required effective capacitance per unit cell that leads to unity effective dielectric constant is

$$C_{\text{period,unity}} = \frac{C_{\text{period}}}{\epsilon_{r,\text{eff}}} = 2.7 \text{ pF}. \tag{4}$$

For the sake of achieving FW phase velocity while avoiding backward propagation, the effective dielectric constant has to be between 0 and 1, which leads to that the total effective capacitance, C_{total}, as shown in Fig. 1, must be smaller than $C_{\text{period,unity}}$, but remain positive. This is expressed as

$$0 < C_{\text{total}} = C_{\text{period}} + (-C_{\text{neg}}) < C_{\text{period,unity}} \tag{5}$$

where $-C_{\text{neg}}$ is the loaded negative capacitance in Fig. 1. Taking $C_{\text{period}} = 10.0$ pF and $C_{\text{period,unity}} = 2.7$ pF, the loaded negative capacitance, $-C_{\text{neg}}$, should be between -10.0 and -7.3 pF. To verify the analytical theory, the phase delays of a three-unit-cell loaded microstrip line, as shown in Fig. 1, are calculated based on (2), with $-C_{\text{neg}}$ equal to -7, -8.5, and -9.5 pF, respectively. The phase delays for the different values of $-C_{\text{neg}}$ are compared to the phase of light passing through the vacuum of the same distance (black solid curve with triangle markers) in Fig. 3. It is clear that the phase-delay curves are above the light curve when the $-C_{\text{neg}}$ is less than

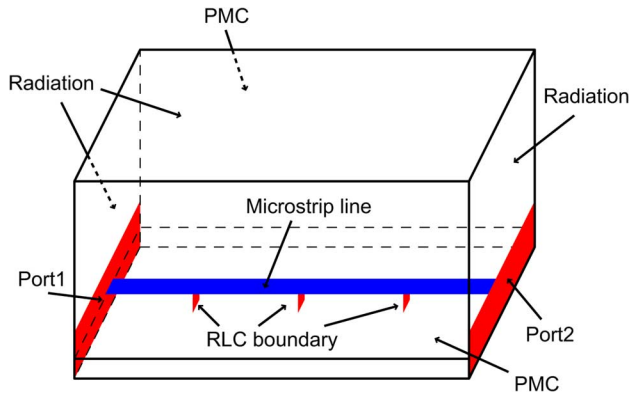

Fig. 2. Numerical simulation model of the proposed periodically loaded transmission line.

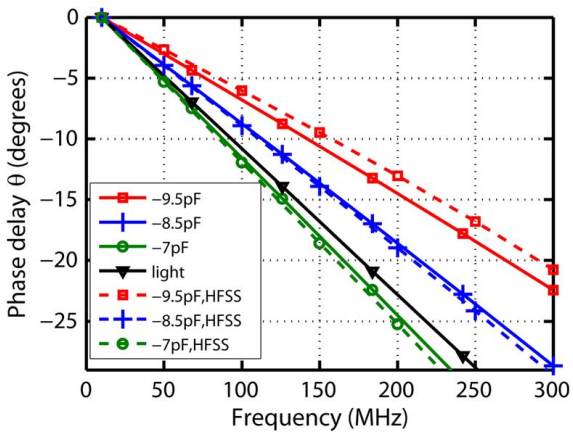

Fig. 3. Phase delay versus frequency for the cases of different lossless negative capacitors. Dashed lines are EM simulation results and the solid lines are the analytical results based on (2). Different colors are the results with different loading capacitance. The black solid line with triangle marker is the phase delay of light traveling through the same distance in free space.

-7.3 pF implying FW propagation, whereas drops below the light line when the $-C_{\rm neg}$ increases to -7 pF, which follows what we have defined for the range of $-C_{\rm neg}$ required by the FW propagation.

A simulation for the same structure is obtained from the finite-element-method-based EM simulator. As shown in Fig. 2, the arbitrary load impedance was realized with a lumped boundary in the simulation. Wave ports were placed at both ends of the microstrip line. The walls on either side of the microstrip line were terminated with perfect magnetic conductor boundaries, and all the remaining faces were defined as radiation boundaries. The simulation results are also presented in Fig. 3 (dashed curves). Both analytical and simulated results are in good agreement, and present FW propagation when $-C_{\rm neg}$ are within proper range.

Practically, negative capacitors implemented with active circuits have finite Q. This effect is investigated by replacing (3) with

$$Y_L = -j\omega C_{\rm neg}\left(1 + j\frac{1}{Q}\right), (C_{\rm neg} > 0) \tag{6}$$

and substituting it into (2). Fig. 4 shows the resultant phase delay associated with $-C_{\rm neg}$ of -9.9 pF and different Q values. It is

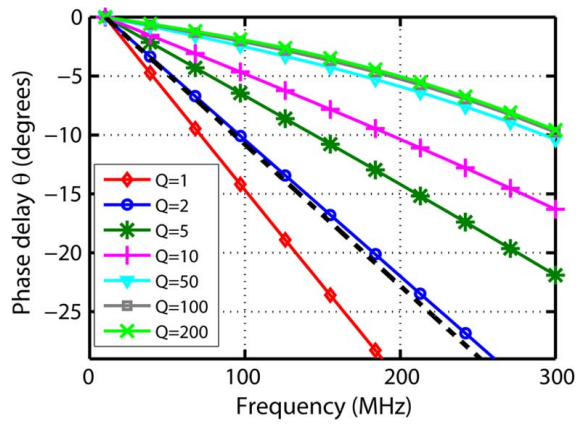

Fig. 4. Phase delay versus frequency for the cases of loading capacitor with various Q. The curves with different colors and markers refer to different Q. The black dashed line refers to the propagation with the speed of light in free space.

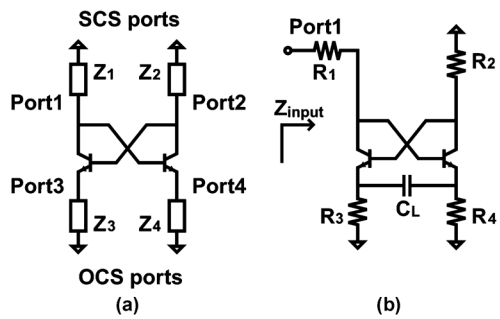

Fig. 5. Transistor-based NIC circuit. (a) General topology of the NIC circuit. (b) Proposed NIC circuit topology.

found that the finite Q affects the phase velocity. Specifically, the phase velocity has a negligible difference when Q is above 50, whereas it gets smaller as loss increases and drops below c when Q is below 2. As discussed in the following section, the active circuit that functions as a negative capacitor has a finite Q so it limits the bandwidth of the FW propagation.

III. Negative Capacitor Realized by a Transistor-Based Negative Impedance Converter (NIC) Circuit

Negative capacitors are classified as non-Foster circuits with reactance having negative frequency slope and impedance locus that goes counter clockwise on a Smith chart [9].

NIC and negative impedance inverter (NII) circuits have been proposed for implementing non-Foster elements [16]–[20]. The conventional basic circuit schematic consisting of two cross coupled transistors is drawn in Fig. 5(a). The input impedance at any of the four ports can be easily calculated as a function of the attached loads at the other three ports. For example, the input impedance at port 1 is expressed as

$$Z_{\rm input1,scs} = -\frac{Z_3 Z_4}{Z_2}. \tag{7}$$

If Z_3 and Z_2 are resistors and Z_4 is a capacitor, (7) implies that the NIC converts a capacitor (Z_4) into a negative capacitor with a multiplicative factor determined by Z_2 and Z_3. This port at the base–collector junction is defined as a short circuit stable (SCS) port. One can find another type of port, i.e., an open circuit stable

(OCS) port, by taking one of the emitters as the input port. The corresponding input impedance can be expressed as [16]

$$Z_{\text{input3,ocs}} = -\frac{Z_1 Z_2}{Z_4}. \tag{8}$$

The definitions of OCS and SCS ports are based on the external loading conditions as required for the stability. For an OCS circuit, the load impedance must be greater than the magnitude of the converted negative impedance, whereas the SCS circuit requires the load impedance to be smaller than the magnitude of the converted negative impedance.

The first challenge in the design of an NIC/NII circuit is to decide which port is appropriate. Since the negative capacitor circuit is intended to just partially compensate for the effective capacitance of the microstrip line for this particular FW application, the magnitude of the negative capacitance must be smaller than the effective capacitance. This means the load impedance (i.e., the impedance corresponding to the effective capacitance of the microstrip line) must be smaller than the generated negative impedance (i.e., the input impedance of the designed NIC circuit). Therefore, the SCS port is chosen for the circuit design.

Another issue in the design is about the components variation and the parasitics in the circuit, which includes the parasitics of the transistors, discrete components, and printed circuit boards (PCBs). These variations and parasitics make it harder to explicitly express the input impedance as a simple equivalent capacitance. As a result, the input impedance is no longer a constant (frequency independent) negative capacitance, but instead is a bandwidth-limited non-constant negative capacitance, even with negative resistance. In order to overcome these effects of the variations and the parasitics, a modified topology has been proposed. As shown in Fig. 5(b), an additional capacitor C_L is placed across the two emitters. Different from the conventional three-load topology [10], [18], the three loads, Z_2, Z_3, and Z_4 in the new circuit are used for stability and dc biasing. Additionally, the negative capacitance of the proposed configuration is mainly determined by C_L. This feature significantly alleviates the components variation and the parasitics effects from the other lumped components, the layout, and the transistors (except the package lead inductance), making the resultant negative capacitor much less sensitive to the unexpected components and fabrication deviation than the conventional NIC circuits.

In addition, using the proper port alone does not guarantee the stability. Since the NIC has a positive feedback circuit, the loop gain may become too large due to the unexpected parasitics. Thus, local oscillations may still exist within the circuit. In the practical circuit design, Z_2, Z_3, and Z_4 were carefully chosen to avoid local oscillations. Additional resistance was also added to the feedback loop in order to reduce the loop gain. In the simulation, accurate component models were utilized to include parasitics of the components.[1] The parasitics of the critical paths on the PCBs were extracted from the EM simulation. The stability was examined by using co-simulation techniques with both time- and frequency-domain stability analysis [21]–[26].

The designed circuit was fabricated on a 5-cm^2 PCB with an FR-4 substrate, as shown in Fig. 6. An Avago transistor

[1][Online]. Available: http://www.modelithics.com/

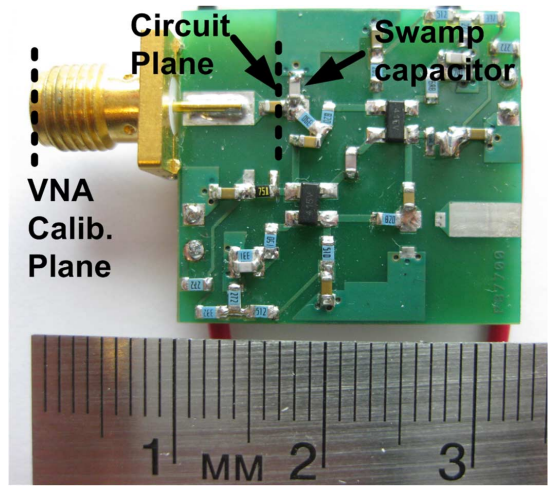

Fig. 6. Fabricated circuit. The VNA calibration plane and circuit plane are used for de-embedding the NIC input impedance.

AT-41511 was adopted. In order to maintain the stability, a positive and large enough swamping capacitor was employed [17], [18]. A two-step measurement technique was used for accurately measuring the negative capacitance. The first step is to measure the swamping element alone. The admittance of this swamping element, Y_{swamp}, is obtained by de-embedding the measured one-port S-parameters from the vector network analyzer (VNA) (Agilent E5071C) calibration plane to the circuit plane, as indicated in Fig. 6. The second step is to measure the S-parameters of the NIC circuit together with the swamping capacitor following the same de-embedding approach, and it is denoted as $Y_{\text{NIC,swamp}}$. The input admittance of the NIC circuit alone is obtained by subtracting the two as

$$Y_{\text{NIC}} = Y_{\text{NIC,swamp}} - Y_{\text{swamp}}. \tag{9}$$

In the measurement, the stability was checked by monitoring any self-oscillations from dc to 10 GHz with a signal analyzer (EXA, Agilent N9010A). Apparently, the stability is guaranteed, which leads to further measurement and study.

The simulation and measurement results with a 10-pF loaded capacitor biased at 10.5 V are presented in Fig. 7. It can be summarized from Fig. 7 that the active circuit produces an equivalent capacitance, C_{NIC}, of -10 pF from 10 to 150 MHz (blue curves in online version). The achieved C_{NIC} varies within the range of 1 pF over the bandwidth of interest. The circuit has the maximum Q factor around 75 MHz and drops below 1 after 150 MHz (red curves in online version). Besides, the conclusion from the measured results (solid curves) is affirmed by the simulation results (dashed curves). The discrepancies in equivalent capacitance and Q factor are due to extra parasitics, which were not included in the co-simulation.

The tunability of the negative capacitor circuit has also been investigated. The generated C_{NIC} can be tuned in two ways, which are: 1) by tuning the biasing voltage of the circuit and 2) by varying the loaded capacitor C_L. Although the capacitor C_L is changed manually in this measurements, it can be tuned with a varactor under careful consideration of the loss and parasitics [10]. The tunability of the circuit is presented in Fig. 8. From

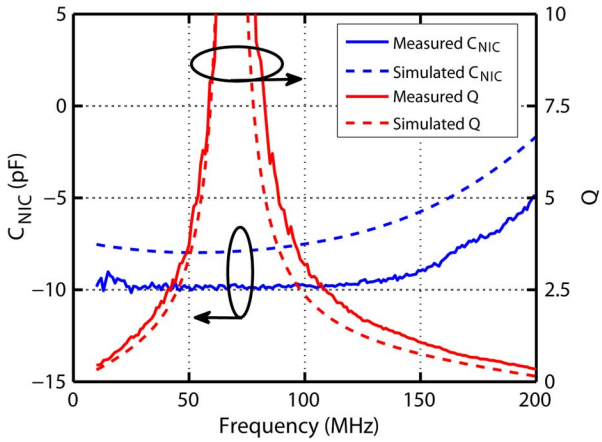

Fig. 7. Equivalent capacitance of the developed NIC circuit with a loaded capacitor of 10 pF biased at 10.5 V and its quality factor. The solid lines are measurement results and the dotted lines are the simulation results.

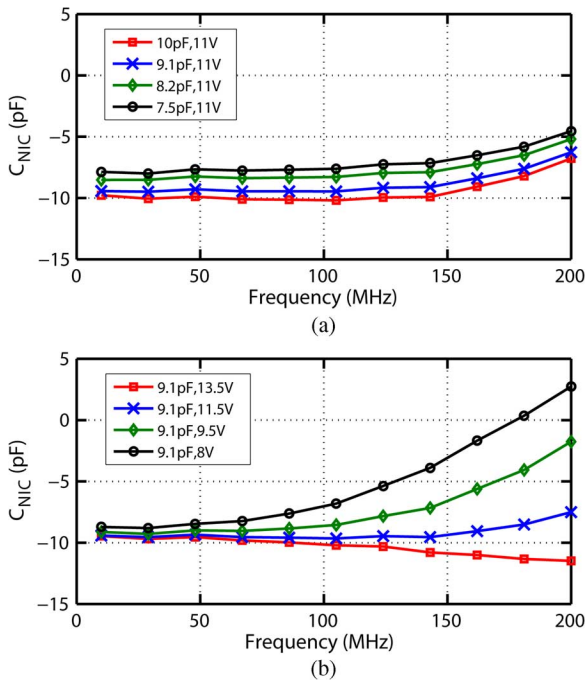

Fig. 8. Tunability of the designed NIC circuit. (a) C_{NIC} with same biasing voltage and different load capacitance. (b) C_{NIC} with the same load capacitance and various biasing voltages.

Fig. 8(a) where the dc bias was fixed and the C_L was tuned, it is found that the C_L determines the C_{NIC} when the dc bias is fixed, and slightly affects the slope of the C_{NIC}, whereas Fig. 8(b) illustrates that the slope of the C_{NIC} is strongly dependent on the dc bias. In particular, an optimum range of the dc voltages is required for a wider bandwidth and a smaller variation in the C_{NIC} over frequency. This feature is exploited in our following design since the change in C_{NIC} with frequency is helpful in compensating for the deviation of the phase velocity due to the finite Q problem.

The bandwidth and consistency of the capacitance for different tuned values are limited mainly due to the inductive parasitics in the circuit. It is possible to achieve better performance if more advanced transistors or IC technology is adopted. The

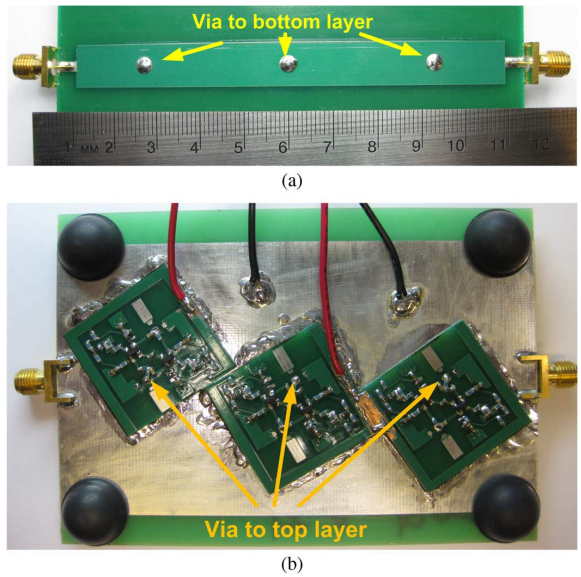

Fig. 9. Fabrication of a three-unit-cell FW waveguide. (a) Top view. (b) Bottom view.

low Q of the negative capacitor also stems from the parasitics. In addition, the low Q is a result of the compromise needed to achieve stability, as a finite amount of loss is incorporated into the circuit to reduce loop gain for stability.

IV. Implementation of The FW Waveguide

A. Fabrication and S-Parameter Measurement

The waveguide studied in Section II has been accomplished with the designed negative capacitor circuits. Fig. 9 illustrates how the FW waveguide is fabricated, where three circuit copies of the same negative capacitor design are integrated to a microstrip line with the width of 10 mm and periodicity of 33 mm on the FR-4 substrate. Three vias on the microstrip line are used to connect to the active circuits. The circuit also has a via at the junction where the swamping capacitor is connected. The circuit and microstrip line are soldered back-to-back.

A co-simulation for the measurement setup was done with an EM model of the microstrip line configured with the same manner as described in Section II, where the lumped boundaries were replaced with a via structure and a 50-Ω lumped port.

In the measurement, the stability of the setup was investigated first. In addition to the methods described in Section III, a single-tone RF signal was injected into one port, the EXA was used to see if any spurious modulated frequencies were detected at the other port. After the stability was guaranteed, a two-port S-parameter measurement of the fabricated waveguide was performed. The phase delay θ and the group velocity (v_g) were calculated from the measured S_{21}, as

$$\theta = \angle S_{21} \tag{10}$$

and

$$v_g = -\frac{L}{\frac{\partial\theta}{\partial\omega}} \tag{11}$$

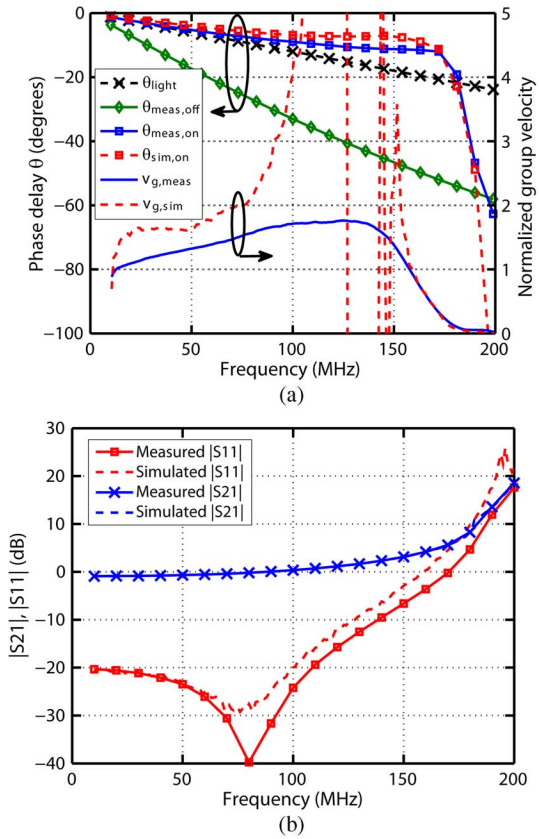

Fig. 10. S-parameter measurement of the designed three-unit-cell FW propagation structure. Dashed lines are simulated results and solid lines are measurement results. (a) Phase of S_{21} and the normalized group velocity. (b) Transmission and reflection coefficient.

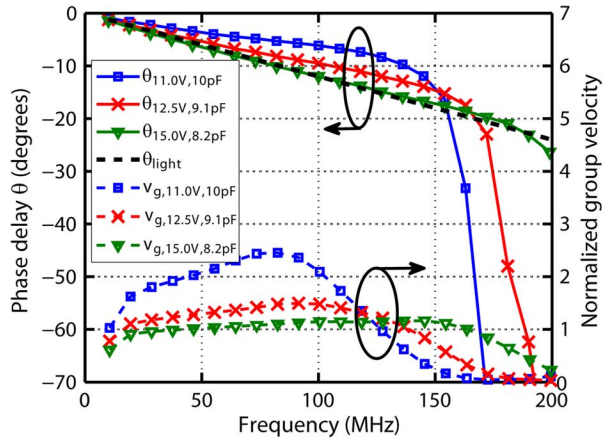

Fig. 11. Tunability of the three-unit-cell FW propagation structure.

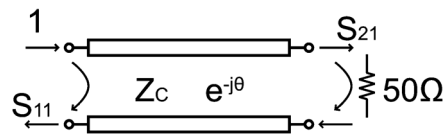

Fig. 12. Effective homogeneous material under S-parameter measurement.

where $L = 100$ mm is the length of the developed waveguide. The phase delay θ and the normalized group velocity v_g to c with the C_L of 9.1 pF at 13-V biasing voltage are extracted and plotted in Fig. 10.

Fig. 10(a) plots the phases of S_{21} and the normalized group velocity. The phases of S_{21} with power on (square markers) and off (diamond markers) are compared to the phase delay of light in vacuum through the same distance (black dashed curve with cross markers). It can be seen that the phase velocity of the waveguide is slower than c when powered off and faster when powered on. Fig. 10(b) is the transmission (S_{21}, red curves in online version) and the reflection (S_{11}, blue curves in online version) of the fabricated waveguide. The reflection is well below -10 dB over the frequency of interest, indicating good match. The transmission coefficient is almost 0 dB below 100 MHz and even presents gain above 100 MHz, which is due to the negative resistance of the loaded non-Foster circuits. The maximum gain is about 25 dB near 200 MHz. It should be noted that the circuit is still stable even with reflection and transmission both greater than unity. A discrepancy between simulation and measurement is observed, which is caused by the parasitics from the manual soldering and fabrication.

The tunability of the three-unit-cell FW structure is studied in Fig. 11, where three different velocities are obtained by biasing the circuit with different voltages and tuning the load capacitance. The measured tunability results show that the fabricated structure can produce the phase velocity varying from c to $2c$, which can potentially be applied in controlling the phase delay of a guided wave device, such as the feeding system of the phased-array antennas. Additionally, it is seen that the bandwidth changes with the tuning, which is because that the bandwidth of the $C_{\rm NIC}$ changes with frequency, as seen from Fig. 8. Therefore, the performance of the waveguide relies on the performance of the negative capacitor circuits.

B. Retrieving the Parameters for Effective Homogeneous Medium

The measured S-parameter in Fig. 10 is the transmission and reflection between the two-port network when the developed waveguide is considered as a two-port network with 50-Ω termination, as shown in Fig. 12. If this two-port network is considered as an effective homogeneous material, which is represented by its characteristic impedance Z_c and phase delay θ, these parameters can be retrieved from the measured S-parameters as [27]

$$Z_c = 50 \times \left(\pm \sqrt{\frac{(1+S_{11}^2)^2 - S_{21}^2}{(1-S_{11}^2)^2} - S_{21}^2} \right) \tag{12}$$

and

$$e^{j\theta} = \frac{S_{21}}{1 - S_{11}\frac{Z_c - 50}{Z_c + 50}}. \tag{13}$$

The plus or minus sign in (12) will be determined by the following two rules: 1) the correct sign should make the real part of Z_c positive and 2) the consistency between the resultant imaginary part of θ and the magnitude of S_{21} should be maintained. This is because Z_c only indicates the ratio of the E- to H-field (or voltage to current), but does not determine the passivity of the material, which, actually, is dictated by the imaginary part

of θ. Since the real part of θ indicates the phase propagation, whereas the imaginary part is the loss of the effective material, the phase velocity can be derived as

$$v_p = -\frac{\omega L}{\theta_r} \tag{14}$$

where θ_r is the real part of the phase delay θ obtained from (13) and L is the total length of the effective homogeneous material, which is 100 mm. The group velocity v_g of the effective material is associated with the derivative of the θ_r to the angular frequency, as stated in (11).

The results of the retrieved phase delay θ and the normalized phase velocity v_p are shown in Fig. 13(a), where faster-than-light phase velocity can be observed over the bandwidth of 50–150 MHz. Fig. 13(b) presents the retrieved loss of the homogeneous material from the imaginary part of θ, which implies less than 1 dB loss below 100 MHz. We can even see gain above 100 MHz due to the negative resistance from the active loads. The consistency between the magnitude of S_{21} in Fig. 10(b) and the loss factor in Fig. 13(b) validates the retrieved results, which presents an effective low-loss FW material over a bandwidth of 50–150 MHz. Furthermore, a stationary phase velocity about $1.2c$ is observed at 90 MHz in Fig. 13(a), indicating perfect dispersionless FW propagation. In particular, the effective bandwidth is 60–120 MHz (i.e., 2:1 bandwidth) by taking 10% variation around $1.2c$.

It should be noticed that the bandwidth of the achieved FW propagation is limited within the RF frequency band. This limitation is attributed to the following effects.

- As discussed in Section II, when the Q of the negative capacitor drops below 2, the phase velocity dramatically decreases. Thus, the most important limiting factor is the finite Q of the negative capacitor circuit.
- The parasitics of the circuit also lead to additional dispersion, causing extra variation in v_p.

These two problems can be solved by adopting application-specific integrated-circuit (ASIC) technologies, where the parasitics are reduced so that it would not affect the functionality at relatively low frequency. Additionally, according to theory of the periodic structure, it should be pointed out that the dispersion is significant if the period is large compared to the operating wavelength. However, this is not the main reason for the limited bandwidth of the realized structure in this paper.

C. Discussion on Relativity, Stability, and Causality

Although it is seen that both phase and group velocity in Fig. 13(a) are larger than the speed of light, Einstein's theory of special relativity is still satisfied. This is because the "superluminal" propagation is obtained over a limited bandwidth, whereas the beginning and ending parts of any meaningful information, which are described with the step function, contain spectrum spreading over the entire frequency range. Therefore, the velocity of the start and end of the information cannot exceed c. To put it another way, as discussed in [11], [12], and [28], the speed of the information is determined by the "precursor velocity" or the "front velocity" rather than the group velocity, and they are never faster than c. However, the "precursor velocity"

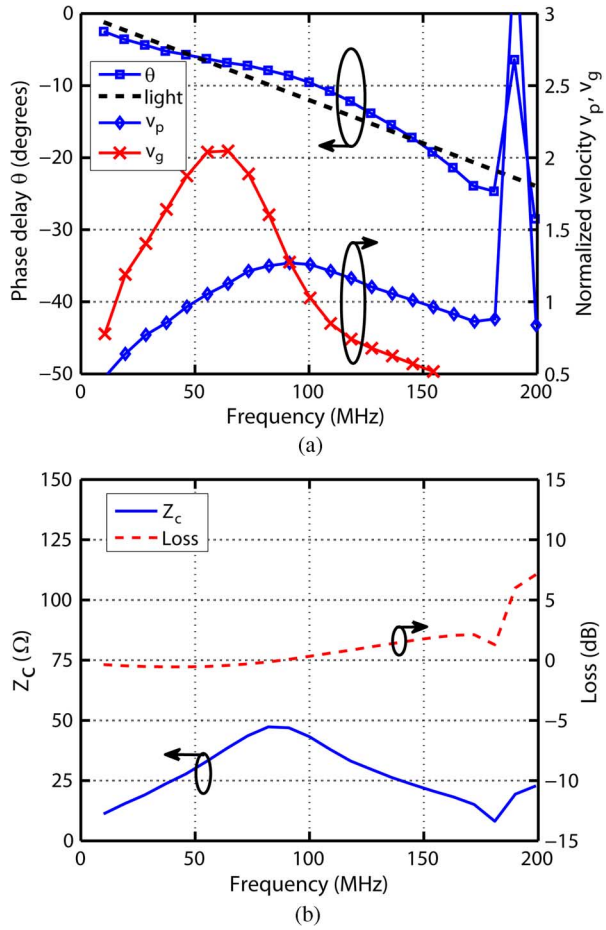

Fig. 13. Retrieved effective propagation parameters. (a) Normalized phase velocity, normalized group velocity, and phase delay compared to light passing through the same distance in free space. (b) Transmission loss and characteristic impedance.

or the "front velocity" argument can not clearly and comprehensively answer the question of whether a band-limited "superluminal" propagation exists or not, and thus it is still an open question calling for further scientific debate.

Regarding the stability and causality, if the system is stable and causal, the magnitude and the phase of the system response must follow Kramers–Kronig relations [28], [29] as

$$\phi(\omega) = -\frac{1}{\pi} P_v \int_{-\infty}^{+\infty} \frac{\ln\left(G(\omega')\right)}{\omega' - \omega} d\omega' \tag{15}$$

where $\phi(\omega)$ and $G(\omega)$ are the phase and magnitude of a system response, respectively. In order to verify the causality and stability of this system, the magnitude of the measured S_{21} from dc to 10 GHz were applied to (15), the calculated phase (dashed red curve in online version) is compared with the measured phase of S_{21} (solid blue curve in online version) in Fig. 14, which clearly shows the agreement between the calculated and measured results, indicating that the developed system is causal and stable.

D. Near-Field Distribution Along the Waveguide

In order to further verify that the developed FW waveguide indeed represents an effective homogeneous medium rather

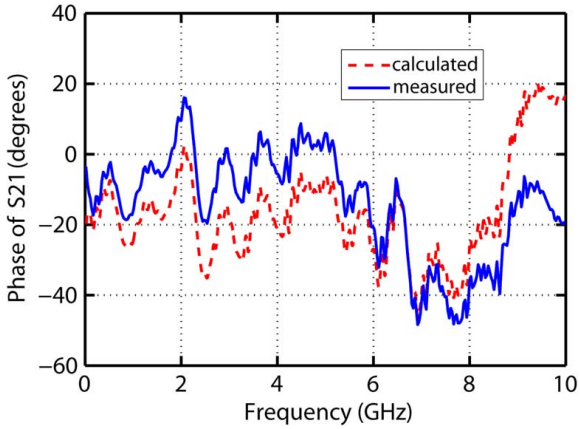

Fig. 14. Comparison of the measured phase of S_{21} (solid blue in online version) to calculated results (dashed red in online version) based on Kramers–Kronig relations.

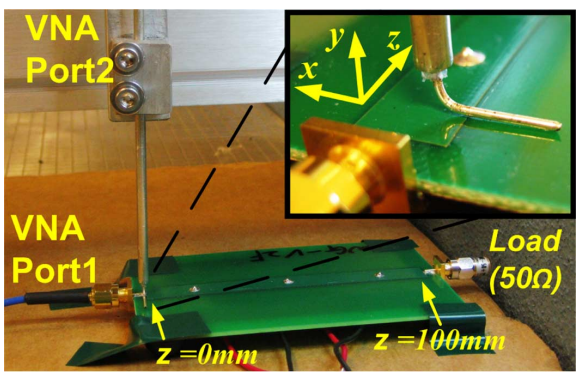

Fig. 15. Configuration of the near-field measurement setup. The probe is scanned along the microstrip line to obtain the phase as a function of position.

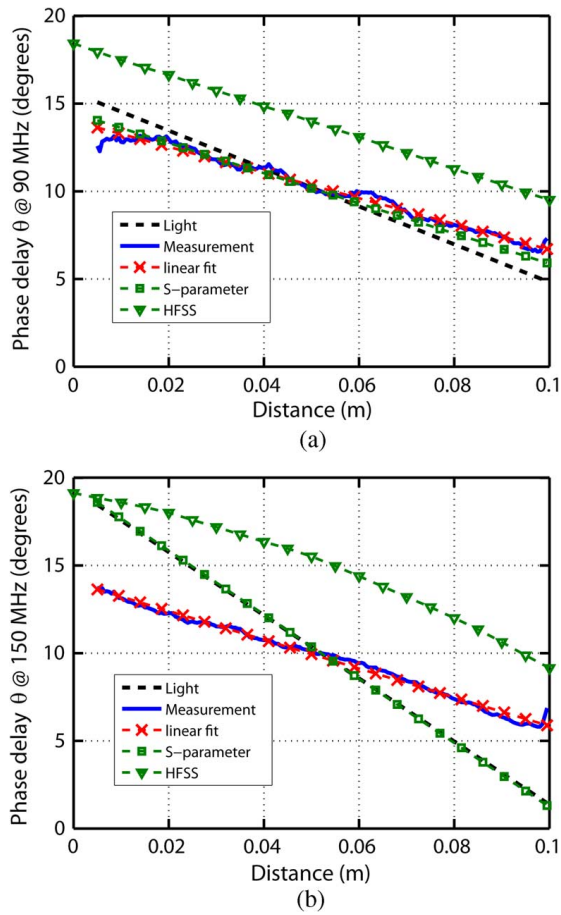

Fig. 16. Field measurement results at: (a) 90 and (b) 150 MHz. Blue solid curve (in online version) is the measured phase of the coupled field along the microstrip line, and the red dashed curve (in online version) with cross markers is the linear fitting result to the measured field. They are compared to the green dashed curve (in online version) with square markers, which is the result derived from retrieved phase velocity. The EM simulation result (green dashed curve in online version, marked with triangle) is used to verify the measured field.

than a lumped element, the near-field distribution along the microstrip line has been measured and analyzed. Fig. 15 illustrates the near-field measurement setup, where one port of the microstrip line is connected to port-1 of the VNA and the other port is terminated with a matched load. A field detector probe mounted on a 1-D positioner sweeps along the microstrip line (z-direction in Fig. 15) and measures the electric field. The phase of the coupled power is extracted and presented in Fig. 16.

The phases of the near field along the waveguide are derived with four approaches and compared in Fig. 16 including: 1) the phase of the raw measured near field; 2) the linear fitted phase from the raw near-field data; 3) simulated phase from EM simulation; and 4) the calculated phase based on the retrieved parameters of the material. The phase of the raw measured data (blue solid curve in online version) is obtained directly from the measurement, and thus, is noisy. The linear fitted phase (red dashed curve in online version, with cross markers) is derived by fitting the raw data with the first-order linear function in order to extract the slope of the phase variation along the waveguide. The simulated phase (green dashed curve in online version, with triangle markers) is from the same EM model described in Section III. The calculated phase (green dashed curve in online version, with square markers) is extrapolated by

$$\theta = -\frac{2\pi f}{v_p} z \tag{16}$$

where v_p is the retrieved phase velocity from (14) at a particular frequency f and z is the distance from the port connected to the VNA to the position of the probe.

Fig. 16(a) and (b) is the comparison at two frequencies, i.e., 90 and 150 MHz, respectively. It is seen that the results at 90 MHz in Fig. 16(a) shows great consistency among the four phases to be compared, supporting the validity of each other. Moreover, compared to the theoretical phase variation of the light in vacuum (black dashed curve), the four phase results all present less slope than the light, which implies FW propagation. By contrast, near-field results deviate from the calculated results at 150 MHz in Fig. 16(b), but still keep coherence with the EM simulation. This is because of the change in the frequency-dependent characteristic impedance, which can be seen in Fig. 13(b) that the characteristic impedance is around 50 Ω near 90 MHz and deviates at other frequencies. To put it another way, the result in Fig. 16(a) is with a good matching condition, which indicates that the field in the transmission line is mainly from a propagating wave. Whereas the result in Fig. 16(b) is under the condition of large impedance mismatch, the field distribution is thus the result of the superposition of multi-reflected waves or a standing wave.

To conclude this part, the field measurement is valid only when the characteristic impedance is matched to the load. The results within the 50-Ω frequency range show good agreement with the retrieved results in Section IV-B. Although the three-unit-cell structure is relatively short compared to the wavelength, the continuously changing of the phase along the waveguide without any abrupt jumps implies that the waveguide can be considered as a homogeneous medium rather than a lumped element, and this has been demonstrated by different methods including analytical calculation, EM simulation, and measurements. The design of a longer FW waveguide with more unit cells is ongoing, which can open many possibilities in the broadband beam-squint-free leaky-wave antenna and active thin-film metasurface for cloaking [2].

V. Conclusion

This paper has reported on the implementation of an FW propagation medium over a bandwidth of 50–150 MHz. The FW structure has been accomplished by a transmission line periodically loaded with transistor-based non-Foster circuits. A novel transistor-based non-Foster circuit has been proposed for better engineering the negative capacitor. The designed circuit exhibits -10-pF negative capacitance over a bandwidth from 10 to 150 MHz. Three such non-Foster circuits have been attached to a transmission line and the S-parameters of the fabricated waveguide have been measured. The retrieved material parameters from the measured S-parameter of the developed waveguide characterize an effective homogeneous material with constant phase velocities about $1.2c$ over a bandwidth of 60–120 MHz, which has been further verified by Kramers–Kronig relations and the near-field measurement. This design has shown the possibility of cascading multiple unit cells and making a causal, a stable, and an effective homogeneous FW material with transistor-based non-Foster circuits. The proposed structure can be applied to a broadband beam-squint-free leaky-wave antennas and cloaking.

References

[1] A. A. Oliner and D. R. Jackson, "Leaky-wave antennas," in *Antenna Engineering Handbook*, 3rd ed. New York, NY, USA: McGraw-Hill, 1993, ch. 10.

[2] D. F. Sievenpiper, "Superluminal waveguides based on non-Foster circuits for broadband leaky-wave antennas," *IEEE Antennas Wireless Propag. Lett.*, vol. 10, pp. 231–234, 2011.

[3] W. Menzel, "A new travelling wave antenna in microstrip," *(AEU) Arch. Elektr. Uebertrag.*, vol. 33, no. 4, pp. 137–140, Apr. 1979.

[4] A. Grbic and G. V. Eleftheriades, "Leaky cpw-based slot antenna arrays for millimeter-wave applications," *IEEE Trans. Antennas Propag.*, vol. 50, no. 11, pp. 1494–1504, Nov. 2002.

[5] S. Lim, C. Caloz, and T. Itoh, "Metamaterial-based electronically controlled transmission-line structure as a novel leaky-wave antenna with tunable radiation angle and beamwidth," *IEEE Trans. Microw. Theory Techn.*, vol. 53, no. 1, pp. 161–173, Jan. 2005.

[6] D. Schurig, J. Mock, B. Justice, S. Cummer, J. Pendry, A. Starr, and D. Smith, "Metamaterial electromagnetic cloak at microwave frequencies," *Science*, vol. 314, no. 5801, pp. 977–980, Nov. 2006.

[7] B. Kanté, D. Germain, and A. de Lustrac, "Experimental demonstration of a nonmagnetic metamaterial cloak at microwave frequencies," *Phys. Rev. B, Condens. Matter*, vol. 80, no. 20, Nov. 2009, Art. ID 201104.

[8] B. Edwards, A. Alù, M. E. Young, M. Silveirinha, and N. Engheta, "Experimental verification of epsilon-near-zero metamaterial coupling and energy squeezing using a microwave waveguide," *Phys. Rev. Lett.*, vol. 100, Jan. 2008, Art. ID 033903.

[9] S. Hrabar, I. Krois, and A. Kiricenko, "Towards active dispersionless ENZ metamaterial for cloaking applications," *Metamaterials*, vol. 4, pp. 89–97, 2010.

[10] J. Long, M. Jacob, and D. F. Sievenpiper, "Electronically steerable antenna using superluminal waveguide and tunable negative capacitors," in *Proc. AP-S Int. Symp.*, Chicago, IL, USA, Jul. 2012, pp. 1–2.

[11] S. Hrabar, I. Krois, I. Bonic, and A. Kiricenko, "Negative capacitor paves the way to ultra-broadband metamaterials," *Appl. Phys. Lett.*, vol. 99, no. 25, Dec. 2011, Art. ID 254103.

[12] S. Hrabar, I. Krois, I. Bonic, and A. Kiricenko, "Ultra-broadband simultaneous superluminal phase and group velocities in non-Foster epsilon-near-zero metamaterial," *Appl. Phys. Lett.*, vol. 102, Feb. 2013, Art. ID 054108.

[13] J.-S. Hong and M. J. Lancaster, *Microstrip Filters for RF/Microwave Applications*. New York, NY, USA: Wiley, 2001.

[14] J. A. Kong, *Theory of Electromagnetic Waves*. New York, NY, USA: Wiley, 1975.

[15] D. M. Pozar, *Microwave Engineering*, 2nd ed. New York, NY, USA: Wiley, 1998.

[16] J. G. Linvill, "Transistor negative-impedance converters," *Proc. IRE*, vol. 41, no. 6, pp. 725–729, Jun. 1953.

[17] C. R. White, J. W. May, and J. S. Colburn, "A variable negative-inductance integrated circuit at UHF frequencies," *IEEE Microw. Wireless Compon. Lett.*, vol. 22, no. 1, pp. 35–37, Jan. 2012.

[18] S. E. Sussman-Fort and R. M. Rudish, "Non-Foster impedance matching of electrically-small antennas," *IEEE Trans. Antennas Propag.*, vol. 57, no. 8, pp. 2230–2241, Aug. 2009.

[19] Z. Ning and R. W. Ziolkowski, "Active metamaterial-inspired broad-bandwidth, efficient, electrically small antennas," *IEEE Antennas Wireless Propag. Lett.*, vol. 10, no. 1, pp. 1582–1585, Jan. 2011.

[20] M. M. Jacob, L. Jiang, and D. F. Sievenpiper, "Broadband non-Foster matching of an electrically small loop antenna," in *Proc. AP-S Int. Symp.*, Chicago, IL, USA, Jul. 2012, pp. 1–2.

[21] J. T. Aberle and R. Loepsinger-Romak, *Antennas With Non-Foster Matching Networks*. San Rafael, CA, USA: Morgan & Claypool, 2007.

[22] M. Tian, V. Visvanathan, J. Hantgan, and K. Kundert, "Striving for small-signal stability," *IEEE Circuits Devices Mag.*, vol. 17, no. 1, pp. 31–41, Jan. 2001.

[23] R. D. Middlebrook, "Null double injection and the extra element theorem," *IEEE Trans. Educ.*, vol. 32, no. 3, pp. 167–180, Aug. 1989.

[24] S. D. Stearns, "Non-Foster circuits and stability theory," in *Proc. AP-S Int. Symp.*, Spokane, WA, USA, Jul. 2011, pp. 1942–1945.

[25] S. D. Stearns, "Incorrect stability criteria for non-Foster circuits," in *Proc. AP-S Int. Symp.*, Chicago, IL, USA, Jul. 2012, pp. 1–2.

[26] E. Ugarte-Munoz, S. Hrabar, D. Segovia-Vargas, and A. Kiricenko, "Stability of non-Foster reactive elements for use in active metamaterials and antennas," *IEEE Trans. Antennas Propag.*, vol. 60, no. 7, pp. 3490–3494, Jul. 2012.

[27] X. D. Chen, T. M. Grzegorczyk, B. I. Wu, J. Pacheco, and J. A. Kong, "Robust method to retrieve the constitutive effective parameters of metamaterials," *Phys. Rev. E, Stat. Phys. Plasmas Fluids Relat. Interdiscip. Top.*, vol. 70, no. 1, pp. 016608-1–016608-7, Jul. 2004.

[28] W. Withayachumnankul, B. M. Fischer, B. Ferguson, B. R. Davis, and D. Abbott, "A systemized view of superluminal wave propagation," *Proc. IEEE*, vol. 98, no. 10, pp. 1775–1786, Oct. 2010.

[29] J. Bechhoefer, "Kramers–Kronig, Bode, and the meaning of zero," *Amer. J. Phys.*, vol. 79, no. 10, pp. 1053–1059, Sep. 2011.

Jiang Long (S'11) received the B.S. and M.S. degrees from Zhejiang University, Hangzhou, China, in 2007 and 2010, respectively, and is currently working toward the Ph.D. degree at the University of California at San Diego (UCSD), La Jolla, CA, USA.

His research area is non-Foster circuits in antenna/microwave applications, including non-Foster circuit-loaded active fast-wave (FW) waveguides, broadband metasurfaces, broadband antennas, and active microwave components.

Minu M. Jacob (S'11) received the B.S. degree from the Amrita School of Engineering, Coimbatore, India, in 2009, and is currently working toward the Ph.D. degree at the University of California at San Diego (UCSD), La Jolla, CA, USA.

Her current research interests include non-Foster circuits and their applications in antennas and metamaterials.

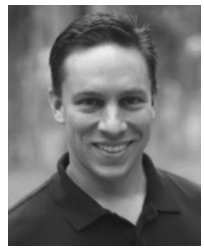

Daniel F. Sievenpiper (M'94–SM'04–F'09) received the B.S. and Ph.D. degrees in electrical engineering from the University of California at Los Angeles (UCLA), Los Angeles, CA, USA, in 1994 and 1999, respectively.

He is currently a Professor with the University of California at San Diego (UCSD), La Jolla, CA, USA, where his research is focused on antennas and electromagnetic (EM) structures. Prior to 2010, he was the Director of the Applied Electromagnetics Laboratory, HRL Laboratories, Malibu, CA, USA, where his research included artificial impedance surfaces, conformal antennas, tunable and wearable antennas, and beam-steering methods. He has authored or coauthored over 60 technical publications. He holds over 70 issued patents.

Dr. Sievenpiper has been an associate editor for the IEEE ANTENNAS AND WIRELESS PROPAGATION LETTERS since 2010. He is currently the chair of the IEEE Antennas and Propagation Society Committee on New Technology Directions. He was the recipient of the 2008 URSI Issac Koga Gold Medal.